



LEARNING TO RECOVER ORIENTATIONS FROM PROJECTIONS IN SINGLE-PARTICLE CRYO-EM

 Jelena Banjac,  Laurène Donati,  Michaël Defferrard
EPFL, Switzerland
{jelena.banjac, laurene.donati, michael.defferrard}@epfl.ch

April 14, 2021

ABSTRACT

A major challenge in single-particle cryo-electron microscopy (cryo-EM) is that the orientations adopted by the 3D particles prior to imaging are unknown; yet, this knowledge is essential for high-resolution reconstruction. We present a method to recover these orientations directly from the acquired set of 2D projections. Our approach consists of two steps: (i) the estimation of distances between pairs of projections, and (ii) the recovery of the orientation of each projection from these distances. In step (i), pairwise distances are estimated by a Siamese neural network trained on synthetic cryo-EM projections from resolved bio-structures. In step (ii), orientations are recovered by minimizing the difference between the distances estimated from the projections and the distances induced by the recovered orientations. We evaluated the method on synthetic cryo-EM datasets. Current results demonstrate that orientations can be accurately recovered from projections that are shifted and corrupted with a high level of noise. The accuracy of the recovery depends on the accuracy of the distance estimator. While not yet deployed in a real experimental setup, the proposed method offers a novel learning-based take on orientation recovery in SPA. Our code is available at <https://github.com/JelenaBanjac/protein-reconstruction>.

1 Introduction

Single-particle cryo-electron microscopy (cryo-EM) has revolutionized the field of structural biology over the last decades [1, 2, 3]. The use of electron beams to image ice-embedded samples has permitted the recovery of 3D bio-structures at unprecedented resolution. This “resolution revolution” has had a tremendous impact in biomedical research, providing invaluable insights into the biological processes that underlie many current diseases.

In single-particle cryo-EM, every 3D particle adopts a random orientation θ_i in the ice layer before being imaged with parallel beams of electrons. Hence, the projection geometry associated to each acquired 2D projection (Figure 1) is unknown. Yet, this knowledge is essential for the tomographic reconstruction of bio-structures [4]. We consider that a cryo-EM measurement (*i.e.*, a projection) $\mathbf{p}_i \in \mathbb{R}^{n_p}$ is acquired through

$$\mathbf{p}_i = \mathbf{C}_\varphi \mathbf{S}_{\mathbf{t}_i} \mathbf{P}_{\theta_i} \mathbf{x} + \mathbf{n}, \quad (1)$$

where $\mathbf{x} \in \mathbb{R}^{n_x}$ is the unknown 3D density map [5] (Coulomb potential). The operator $\mathbf{P}_{\theta_i} : \mathbb{R}^{n_x} \rightarrow \mathbb{R}^{n_p}$ is the projection along the orientation θ_i (*i.e.*, the x-ray transform). The operator $\mathbf{S}_{\mathbf{t}_i} : \mathbb{R}^{n_p} \rightarrow \mathbb{R}^{n_p}$ is a shift of the projection by $\mathbf{t}_i = (t_{i_1}, t_{i_2})$. The convolution operator $\mathbf{C}_\varphi : \mathbb{R}^{n_p} \rightarrow \mathbb{R}^{n_p}$ models the microscope point-spread function (PSF) with parameters $\varphi = (d_1, d_2, \alpha_{\text{ast}})$, where d_1 is the defocus-major, d_2 is the defocus-minor, and α_{ast} is the angle of astigmatism [6, 7]. Finally, $\mathbf{n} \in \mathbb{R}^{n_p}$ represents additive noise. Figure 6 illustrates the effect of projection, shift, and noise. The challenge is then to reconstruct \mathbf{x} from a set of projections $\{\mathbf{p}_i\}_{i=1}^P$ acquired along unknown orientations.

A popular approach is to alternatively refine the 3D structure and an estimation of the orientations [8, 9, 10, 11, 12, 13]. Yet, the outcome of these iterative-refinement procedures is still often predicated on the quality of the initial reconstruction, or, equivalently, on the initial estimation of the orientations [14, 15].

Several methods have been designed to produce a first rough *ab initio* structure for the refinement procedure [16]. An early approach [17] proposed to reconstruct an initial structure such that the first few moments of the distribution of its

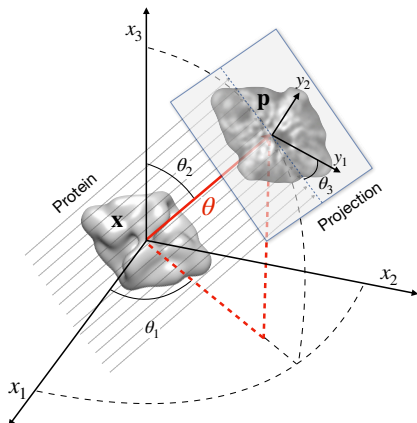


Figure 1: Geometry of the imaging model defined in (1). The 3D density \mathbf{x} in the coordinate system (x_1, x_2, x_3) is imaged along the orientation θ to produce the 2D projection \mathbf{p} in the coordinate system (y_1, y_2) of the microscope’s detector plane. The orientation $\theta = (\theta_3, \theta_2, \theta_1)$ is decomposed as the direction $(\theta_2, \theta_1) \in [0, \pi] \times [0, 2\pi[$ (parameterizing the sphere \mathbb{S}^2) and the in-plane rotation $\theta_3 \in [0, 2\pi[$ (parameterizing the circle \mathbb{S}^1). In our work, we represent the orientation θ as a unit quaternion q .

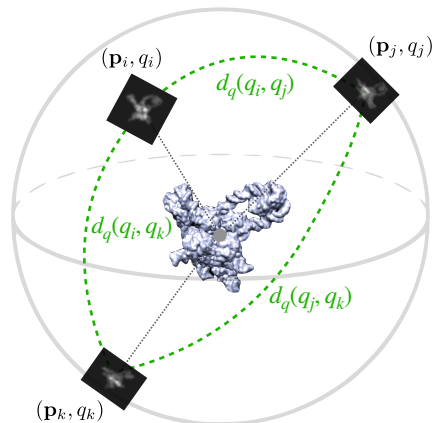


Figure 2: Single-particle cryo-EM produces P projections (with P in the order of 10^5) from unknown orientations: $\{(\mathbf{p}_i, q_i)\}_{i=1}^P$. Observing that distances constrain the latter, we aim to *recover the orientations* $\{q_i\}$ from $\{d_q(q_i, q_j)\}$, where $d_q(q_i, q_j)$ is the distance (angle) between orientations q_i and q_j . Observing that the similarity between projections depends on their relative orientation, we aim to *estimate the distance* $d_q(q_i, q_j)$ from the projections $(\mathbf{p}_i, \mathbf{p}_j)$.

theoretical measurements match the ones of its experimental projections. Since then, *moment-matching* techniques have been refined and extended [18, 19, 20], e.g., to accommodate for non-uniform orientation configurations. However, they typically remain sensitive to error in data and can require relatively high computational complexity.

Another popular approach relies on the central-slice theorem, which relates the Fourier transform of a projection to a plane (orthogonal to the projection direction) in the Fourier transform of the 3D object [4]. Hence, every two projections *de facto* share a common 1D intersection in the 3D Fourier domain, and three projections theoretically suffice to define a coordinate system from which their orientations can be deduced [21]. Exploiting this principle, *common-lines* methods aim at uniquely determining the orientations of each projection by identifying the common-lines between triplets of projections [8, 22, 23, 24, 25, 26]—a real technical challenge given the massive amount of noise in cryo-EM data.

Alternatively, the marginalized maximum likelihood (ML) formulation of the reconstruction problem [11]—classically used for the iterative-refinement procedures themselves—can be minimized using stochastic gradient descent [27]. This permits to avoid the need for an initial volume estimate, at the possible cost of greater convergence instability. More recently, the recovery of geometrical information from unknown view tomography of 2D point sources has been proposed [28], but the extension to 3D cryo-EM tomography is not straightforward. Finally, [29] proposed to embed the in-plane rotations by learning to embed projections in an appropriate latent space, but only after directions had been estimated through three rounds of 2D classification in RELION.

Despite the many aforementioned advances, the task of providing a robust initial volume remains an arduous challenge in single-particle cryo-EM due to the high-dimensionality and strong ill-posedness of the underlying optimization problem. On the other hand, deep learning has had a profound influence in imaging in reason of the remarkable ability of convolutional neural networks to capture relevant representations of images [30].

In this work, we present a new learning-based approach to recover the unknown orientations directly from the acquired set of projections. By doing so, orientations are recovered without the need for an intermediate reconstruction procedure or an initial volume estimate.

2 Method

Our approach relies on two observations (Figure 2), yielding two steps (Figure 3). First, the greater the similarity between two 2D projections $(\mathbf{p}_i, \mathbf{p}_j)$, the more likely they originated from two 3D particles that adopted close orientations (q_i, q_j) in the ice layer prior to imaging;¹ this observation guides a number of applications in the field [2]. Hence, we aim

¹Up to protein symmetries, which we discuss later.

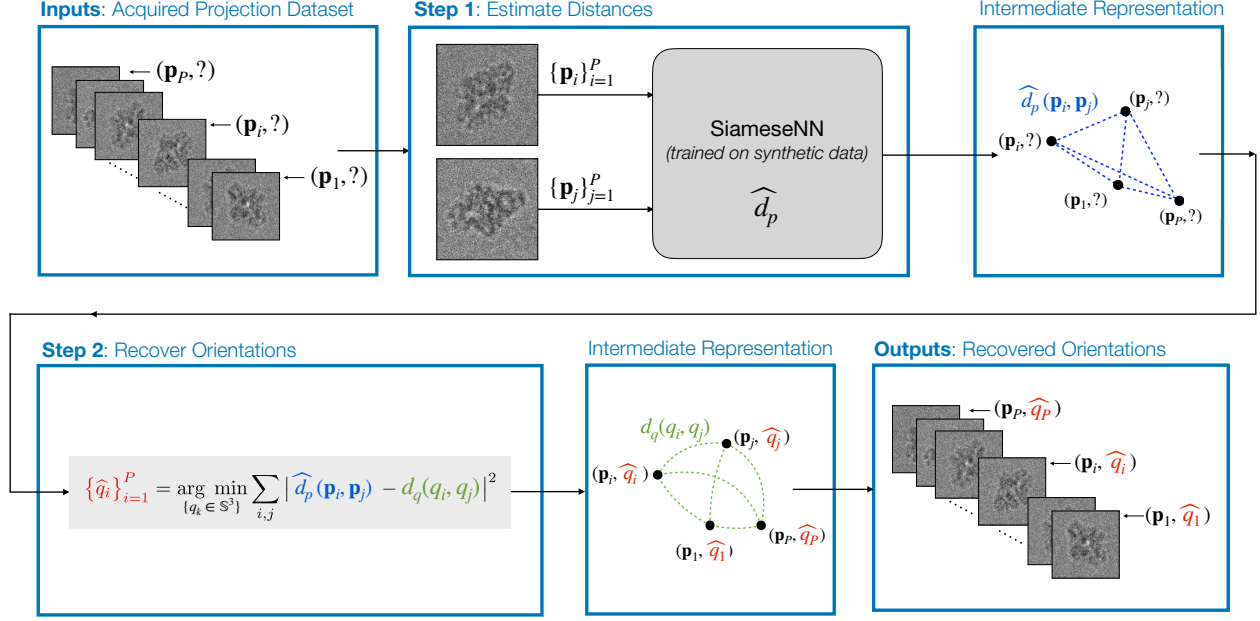


Figure 3: Our method consists of two steps. First, we estimate distances between pairs of projections. Second, we recover the orientation of each projection from these distances.

to *estimate distances* between orientations $d_q(q_i, q_j)$ from the projections themselves as $\hat{d}_p(\mathbf{p}_i, \mathbf{p}_j)$, which we discuss in §2.2. Second, an orientation q is constrained by the distances between itself and the other orientations $\{d(q, q_j)\}$. Hence, we aim to *recover orientations* $\{\hat{q}_k\}$ such that the induced distances $\{d_q(\hat{q}_i, \hat{q}_j)\}$ are close to the estimated distances $\{\hat{d}_p(\mathbf{p}_i, \mathbf{p}_j)\}$, which we discuss in §2.3. All in all, from a set of projections $\{\mathbf{p}_k\}$, we aim to recover their orientations $\{\hat{q}_k\}$ such that $d_q(\hat{q}_i, \hat{q}_j) \approx \hat{d}_p(\mathbf{p}_i, \mathbf{p}_j) \approx d_q(q_i, q_j)$, with equality if \hat{d}_p and $\{\hat{q}_k\}$ are perfectly estimated.

Our approach is similar to [31]. While the authors are there concerned with the reconstruction of 2D images from 1D projections, they rely on the same two-step approach: they (i) estimate distances as $\hat{d}_p(\mathbf{p}_i, \mathbf{p}_j) = \|\mathbf{p}_i - \mathbf{p}_j\|_2$ then (ii) recover the orientations by spectrally embedding that distance graph. The Euclidean distance is however not robust to perturbations: for example, two projections that only differ by a shift \mathbf{S}_t of one pixel would be considered far apart while their orientations are the same. They noted that issue and we observed it too (Appendix C). To circumvent this, we propose to *learn* \hat{d}_p from examples (§2.2).

2.1 Representation of orientations with quaternions

The orientation of a 3D particle with respect to the microscope’s detector plane is a rotation relative to a reference orientation (Figure 1). The group of all 3D rotations under composition is identified with $\mathbf{SO}(3)$, the group of 3×3 orthogonal matrices with determinant 1 under matrix multiplication. A rotation matrix $\mathbf{R}_\theta \in \mathbf{SO}(3)$ can be decomposed as a product of $\binom{3}{2} = 3$ independent rotations, for example as $\mathbf{R}_\theta = \mathbf{R}_{\theta_3} \mathbf{R}_{\theta_2} \mathbf{R}_{\theta_1}$, where $\theta = (\theta_3, \theta_2, \theta_1) \in [0, 2\pi[\times [0, \pi] \times [0, 2\pi[$ are the (extrinsic and proper) Euler angles in the ZYZ convention (a commonly-used parameterization in cryo-EM) [32].

While Euler angles are a concise representation of orientation (3 numbers for 3 degrees of freedom), they suffer from a topological constraint—there is no covering map from the 3-torus to $\mathbf{SO}(3)$ —which manifests itself in the *gimbal lock*, the loss of one degree of freedom when $\theta_2 = 0$. This makes their optimization by gradient descent (§2.3) problematic. On the other hand, the optimization of rotation matrices (made of 9 numbers) would require computationally costly constraints (orthogonality and determinant 1) to reduce the number of degrees of freedom to 3. Moreover, the distance between orientations cannot be directly computed from Euler angles and is costly (30 multiplications) to compute from rotation matrices [33]. We solve both problems by representing orientations with unit quaternions.

Quaternions $q \in \mathbb{H}$ are an extension of complex numbers² of the form $q = a + bi + cj + dk$ where $a, b, c, d \in \mathbb{R}$. Unit quaternions $q \in \mathbb{S}^3$, where $\mathbb{S}^3 = \{q \in \mathbb{H} : |q| = 1\}$ is the 3-sphere (with the additional group structure inherited

²The algebra \mathbb{H} is similar to the algebra of complex numbers \mathbb{C} , with the exception of multiplication being non-commutative.

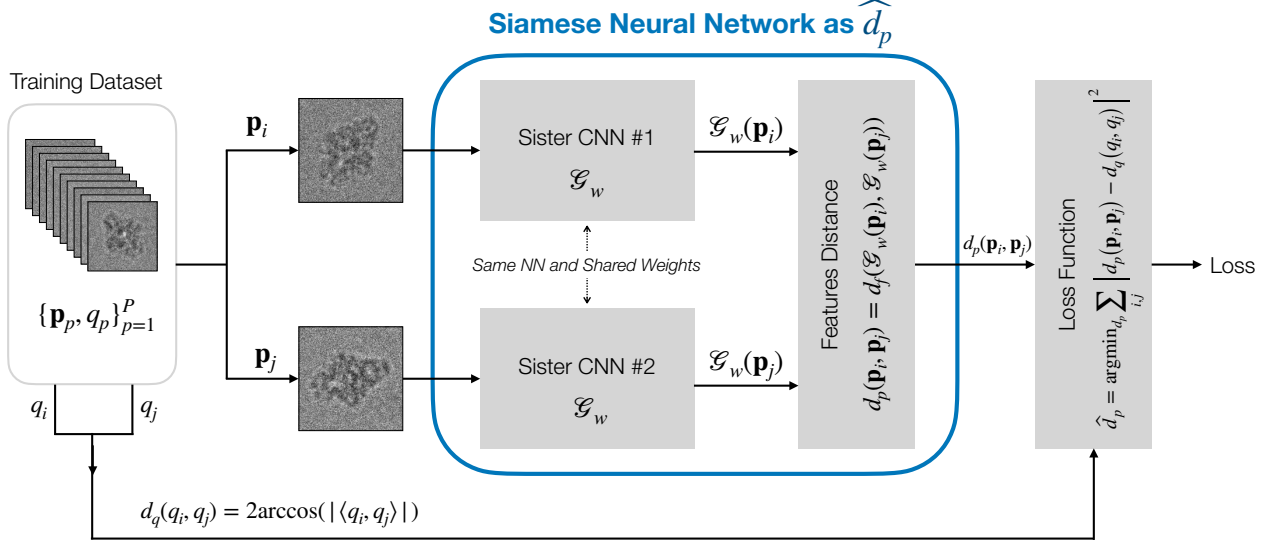


Figure 4: Distance learning. We are looking for a distance \hat{d}_p between projections that is an accurate estimator of the distance d_q between their orientations. We propose to parameterize \hat{d}_p as a Siamese neural network (SiameseNN), trained on a synthetic dataset of projections with associated orientation.

from quaternion multiplication), concisely and elegantly represent a rotation of angle θ about axis (x_1, x_2, x_3) as $q = \cos(\theta/2) + x_1 \sin(\theta/2)\mathbf{i} + x_2 \sin(\theta/2)\mathbf{j} + x_3 \sin(\theta/2)\mathbf{k}$. They parameterize rotation matrices as

$$\mathbf{R}_q = \begin{pmatrix} a^2 + b^2 - c^2 - d^2 & 2bc - 2ad & 2bd + 2ac \\ 2bc + 2ad & a^2 - b^2 + c^2 - d^2 & 2cd - 2ab \\ 2bd - 2ac & 2cd + 2ab & a^2 - b^2 - c^2 + d^2 \end{pmatrix}.$$

Note that $\mathbb{S}^3 \rightarrow \mathbf{SO}(3)$ is a two-to-one mapping (a double cover) as q and $-q$ represent the same orientation. Unlike Euler angles, \mathbb{S}^3 is isomorphic to the universal cover of $\mathbf{SO}(3)$. Hence, the distance between two orientations, *i.e.*, the length of the geodesic between them on $\mathbf{SO}(3)$, is given by

$$d_q : \mathbb{S}^3 \times \mathbb{S}^3 \rightarrow [0, \pi],$$

$$d_q(q_i, q_j) = 2 \arccos(|\langle q_i, q_j \rangle|), \quad (2)$$

where $\langle \cdot, \cdot \rangle$ is the inner product, and the absolute value $|\cdot|$ ensures that $d_q(q_i, q_j) = d_q(q_i, -q_j)$. The distance $d_q(q_i, q_j)$ corresponds to the magnitude (angle θ) of the rotation \mathbf{R}_* such that $\mathbf{R}_{q_i} = \mathbf{R}_* \mathbf{R}_{q_j}$ [33].

2.2 Distance learning

We aim to estimate a function \hat{d}_p such that $\hat{d}_p(\mathbf{p}_i, \mathbf{p}_j) \approx d_q(q_i, q_j)$. While we could in principle design \hat{d}_p , that would be intricate—if not impossible—partly because the invariants are difficult to specify. We instead opt to learn \hat{d}_p , capitalizing on (i) the powerful function approximation capabilities of neural networks, and (ii) the possibility to generate realistic cryo-EM projection datasets supported by the availability of numerous 3D atomic models³ and our ability to model the imaging procedure.

From a training dataset $\{\mathbf{p}_i, q_i\}_{i=1}^P$, we learn the projection distance

$$\hat{d}_p = \arg \min_{d_p} L_{DE}, \quad \text{where} \quad L_{DE} = \sum_{i,j} |d_p(\mathbf{p}_i, \mathbf{p}_j) - d_q(q_i, q_j)|^2 \quad (3)$$

is the loss and d_q is defined in (2). The distance d_p is parameterized as the Siamese neural network (SiameseNN) [34]

$$d_p(\mathbf{p}_i, \mathbf{p}_j) = d_f(\mathcal{G}_w(\mathbf{p}_i), \mathcal{G}_w(\mathbf{p}_j)),$$

where \mathcal{G}_w is a convolutional neural network with weights w that is trained to extract the most relevant features $\mathbf{f}_i \in \mathbb{R}^{r_f}$ from a projection \mathbf{p}_i . SiameseNNs, also termed “twin networks”, are commonly used in the field of deep metric learning

³<https://www.ebi.ac.uk/pdbe/emdb>

to learn similarity functions [35]. We set the feature space distance d_f as the cosine distance to facilitate the learning of a \widehat{d}_p that respects the elliptic geometry of \mathbb{S}^3 (Appendix D). Figure 4 illustrates the proposed learning paradigm.

As evaluating a sum over P^2 pairs is computationally intractable for cryo-EM datasets with typically P in the order of 10^5 projections, we sample the sum and minimize (3) with stochastic gradient descent (SGD) over small batches of pairs. The weights w are updated by back-propagation.

The architecture of \mathcal{G}_w is described in Appendix E. When designing the architecture, we constrain the functional space from which the trained \mathcal{G}_w is drawn and express our prior expert knowledge. For example, we realize shift invariance, *i.e.*, a guarantee that a shift \mathbf{S}_t does not change our estimated distances and orientations, with a fully convolutional architecture. Size invariance, *i.e.*, taking projections \mathbf{p} of varying sizes n_p while yielding a representation \mathbf{f} of a fixed size n_f , is realized by a final average pooling layer. As we do not (yet) know how to realize an invariance to noise or PSF, we resort to data augmentation, *i.e.*, training on perturbed projections. In §3.4, we show that a built-in invariance (shift) is far preferable to one learned through augmentation (noise). Finally, as projections are made by integrating through the 3D volume, projections from opposed directions (θ_2, θ_1) are mirrors of each other.⁴ That is another kind of physical knowledge that should ideally be built into our method.

One could hope to train \mathcal{G}_w to directly map projections to orientations as $\widehat{q}_i = \mathbf{f}_i = \mathcal{G}_w(\mathbf{p}_i)$. While that would avoid the orientation recovery step, a space of $n_f = 4$ dimensions does not have room for \mathcal{G}_w to represent the other factors of variation in \mathbf{p} , such as different noise levels, PSFs, or proteins. We tested that hypothesis in Appendix D.

2.3 Orientation recovery

The task of recovering points based on their relative distances has been extensively studied. Many methods aim at mapping high-dimensional data onto a lower-dimensional space while preserving distances, primarily for dimensionality reduction and data visualization. Well-known examples include multi-dimensional scaling (MDS) [36], Isomap [37], locally linear embedding (LLE) [38], Laplacian eigenmaps [39], t-distributed stochastic neighbor embedding (t-SNE) [40], and uniform manifold approximation and projection (UMAP) [41]. The embedding of distance matrices in Euclidean space (given by their eigenvectors) is especially well-described. In particular, the framework of Euclidean distance matrices (EDMs) [42] provides theoretical guarantees on the recovery of points from distances.

We however aim to embed the orientations q in \mathbb{S}^3 (§2.1), a setting for which we are unaware of any theoretical characterization (*e.g.*, on the shape of the loss function or its behavior when distances are missing or noisy). The fact that \mathbb{S}^3 is locally Euclidean does however offer some hope. Indeed, despite the non-convexity and the lack of theoretical guarantees, we are able to appropriately minimize our loss function, as we experimentally demonstrate in Appendix B.

We recover the orientations of a set of projections $\{\mathbf{p}_k\}_{k=1}^P$ through

$$\{\widehat{q}_k\}_{k=1}^P = \arg \min_{\{q_k \in \mathbb{S}^3\}} L_{\text{OR}}, \quad \text{where} \quad L_{\text{OR}} = \sum_{i,j} \left| \widehat{d}_p(\mathbf{p}_i, \mathbf{p}_j) - d_q(q_i, q_j) \right|^2 \quad (4)$$

is the loss and \widehat{d}_p is the estimator trained in (3). Note that the sole difference with (3) is that the minimization is performed over the orientations q rather than the distance d_p . Here again, we sample the sum in practice and minimize (4) with mini-batch SGD. Sampling the sum amounts to building a sparse (instead of complete) distance graph before embedding, a common strategy.

2.4 Evaluation

While not a part of the method *per se*, the evaluation of the orientations recovered by (4) is essential for assessing the quality of the obtained results. Unfortunately, we cannot directly take the difference between the recovered orientations $\{\widehat{q}_k\}_{k=1}^P$ and the true orientations $\{q_k\}_{k=1}^P$ as orientations are rotations up to an arbitrary reference orientation. Any global rotation or reflection of the recovered orientations is as valid as any other, *i.e.*, $d_q(q_i, q_j) = d_q(\mathbf{T}q_i, \mathbf{T}q_j) \forall \mathbf{T} \in \mathbf{O}(4)$, where $\mathbf{O}(4)$ is the group of 4×4 orthogonal matrices. Hence, we align the sets of orientations and compute the *mean orientation recovery error* as

$$E_{\text{OR}} = \min_{\mathbf{T} \in \mathbf{O}(4)} \frac{1}{P} \sum_{i=1}^P |d_q(q_i, \mathbf{T}\widehat{q}_i)|. \quad (5)$$

⁴That fact prevents cryo-EM reconstruction to resolve chirality, *i.e.*, it cannot distinguish a protein from its mirrored version.

We implement \mathbf{T} as a product of $\binom{4}{2} = 6$ independent rotations and an optional reflection:

$$\mathbf{T} = \begin{bmatrix} m & \mathbf{0} \\ \mathbf{0} & \mathbf{I} \end{bmatrix} \prod_{1 \leq i < j \leq 4} \mathbf{T}_{\theta_{ij}}, \quad m \in \{-1, 1\}, \theta_{ij} \in [0, 2\pi[$$

where $m = \det(\mathbf{T}) = -1$ if \mathbf{T} includes a reflection, and $\mathbf{T}_{\theta_{ij}} \in \mathbf{SO}(4)$ is a rotation by angle θ_{ij} on the (x_i, x_j) plane.

In practice, we again minimize (5) with mini-batch SGD. Because $\mathbf{O}(4)$ is disconnected, we optimize the 6 angles separately for $m = 1$ (proper rotations) and $m = -1$ (improper rotations). Figure 15 shows an alignment to $E_{OR} = 0$ after a perfect recovery.

3 Experiments

We first evaluated whether orientation recovery through (4) was feasible assuming perfect distances, and how it was affected by errors in the distances (§3.2). We then learned to estimate the distances through (3) and evaluated the accuracy of this procedure (§3.3). Following this, we evaluated the robustness of distance learning to perturbations in the projections (§3.4). Finally, we ran the whole machinery on a synthetic dataset to assess how well orientations could be recovered from distances estimated by the trained SiameseNN (§3.5).

3.1 Experimental conditions

Density maps. We considered two proteins (Figure 5): the β -galactosidase, a protein with a dihedral (D2) symmetry, and the lambda excision HJ intermediate (HJI), an asymmetric protein with local cyclic (C1) symmetry. Their deposited PDB atomic models are 5a1a [43] and 5j0n [44], respectively. From these atomic models, we generated the density maps in Chimera [45] by fitting the models with a 1Å map for 5a1a and a 3.67Å map for 5j0n; this gave us a volume of $110 \times 155 \times 199$ voxels for 5a1a and one of $69 \times 57 \times 75$ voxels for 5j0n.

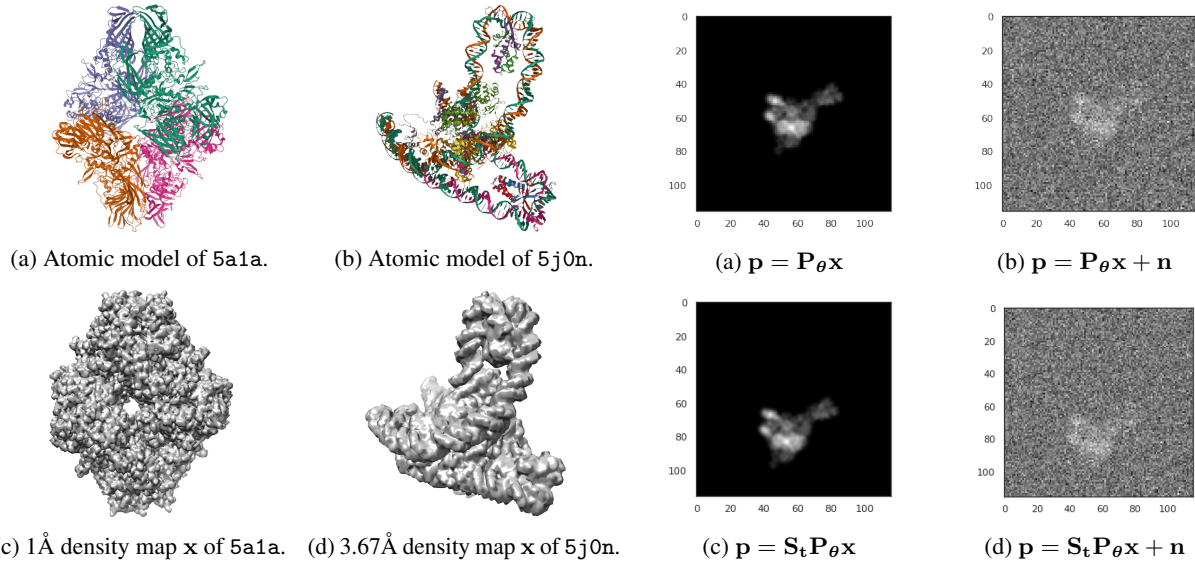


Figure 5: Two proteins with different symmetries.

Figure 6: Example projections of 5j0n ($\mathbf{n} \sim \mathcal{N}(0, 16\mathbf{I})$).

Protein symmetries. Symmetries are problematic when learning distances: two projections can be identical while not originating from the same orientation, which breaks an axiom of proper distance functions (identity of indiscernibles). Figure 16b illustrates this problem. To capture only one of four identical projections of 5a1a, we restricted directions to $(\theta_2, \theta_1) \in [0, \pi[\times [0, \frac{\pi}{2}[$ (a quarter of the sphere, illustrated in Figure 12a) for that protein. This treatment of symmetries is incomplete⁵ but sufficient for a proof-of-concept.

⁵The remaining issue is that one of four distances is arbitrarily chosen per pair of projections.

Projections. Using the ASTRA projector [46], we generated $P = 5,000$ synthetic projections of 275×275 pixels (then interpolated to 116×116) for 5a1a and 116×116 pixels for 5j0n, taken from uniformly sampled orientations.⁶ We then perturbed the measurements with different levels of additive Gaussian noise [47, 48] and off-centering shifts. Figure 6 displays samples of the simulated projections.

Datasets. For each protein, we split the projections into training, validation, and test subsets, and created *disjoint* pairs of projections from each (Table 1). The training and validation sets were used to train and evaluate the SiameseNN, while the test set was used to evaluate orientation recovery given a trained SiameseNN. Sampling orientations (mostly) uniformly induces a distribution of distances that is skewed towards larger distances (shown in Figure 12b). As this would skew L_{DE} and bias \hat{d}_p , we further sampled 1% of the training and validation pairs to make the distribution of distances uniform—for \hat{d}_p to be uniformly accurate over the whole $[0, \pi]$ range of distances (see Appendix A for further illustrations). While 1,650 projections were enough to perfectly reconstruct the density maps (as shown in Figures 11e and 11j), our method is not limited by the number of projections as optimization is done per batch.

Optimization. We optimized (3) with the RMSProp optimizer [49] and a learning rate of 10^{-3} for 150 epochs. Batches of 256 pairs resulted in 247 steps per epoch for the training sets and 28 for the validation sets (Table 1). It took about 3.3 hours of a single Tesla T4 or 8.75 hours of a single Tesla K40c. Our code supports training on multiple GPUs. We optimized (4) with the Adam optimizer [50] and a learning rate of 0.5 until convergence on batches of 256 pairs sampled from the test sets (Table 1). It took about 3.75 hours of a single Tesla K40c (without early stopping). We optimized (5) with the FTRL optimizer [51], a learning rate of 2, and a learning rate power of -2 on batches of 256 orientations sampled from the test sets (Table 1). We reported the lowest of 6 runs (3 per value of m) of 300 steps each. This took about 50 minutes of CPU.

3.2 Sensitivity of orientation recovery to errors in distance estimation

We first evaluated the feasibility of orientation recovery assuming that the exact distances were known. Experiments confirmed that the method successfully recovers the orientation of every projection in this case (see Appendix B).

We then evaluated the behavior of (4) when the true distances were increasingly perturbed. More precisely, we perturbed the distances prior to the minimization with an error sampled from a Gaussian distribution with mean 0 and variances $\sigma^2 \in [0.0, 0.8]$. Figure 7 shows that the recovery error E_{OR} from (5) is a monotonic function of the error in distances: from $E_{OR} = 0$ with perfect distances to $E_{OR} \approx 0.2$ radians ($\approx 11.5^\circ$) for $\sigma^2 = 0.8$. These results demonstrate that the performance of orientation recovery (4) depends on the quality of the estimated distances, which advocates for a proper and extensive training of the SiameseNN in further stages of development.

Moreover, we observe that the loss L_{OR} from (4) is a reliable proxy for E_{OR} , allowing us to assess recovery performance in the absence of ground-truth orientations (*i.e.*, when recovering the orientations of real projections).

3.3 Learning to estimate distances

We evaluated the ability of the SiameseNN to learn to approximate the orientation distance d_q through (3). For comparison, we evaluated a baseline, the Euclidean distance $\hat{d}_p(\mathbf{p}_i, \mathbf{p}_j) = \|\mathbf{p}_i, \mathbf{p}_j\|_2$, in Appendix C.

Figure 8a shows the convergence of L_{DE} , reached in about 50 epochs. Figure 8b shows the relationship between the distance \hat{d}_p estimated from projections and the true distance d_q . The outliers for 5a1a are explained by our incomplete treatment of its symmetry. While our learned distance function is a much better estimator than the Euclidean distance—compare Figure 8b with Figure 16—they share one characteristic: both plateau and underestimate the largest distances. We did attenuate the phenomenon by sampling training distances uniformly (see §3.1), and the issue is much less severe than with the Euclidean distance. An alternative could be to only rely on smaller distances for recovery. That would however require the addition of a spreading term in (4) to prevent the recovered orientations to collapse.

These results confirm that a SiameseNN is able to estimate differences in orientations from projections alone, even though much has yet to be gained from improving upon the rather primitive SiameseNN architecture we are currently using. The use of additional training data should help further diminish overfitting.

⁶Orientations used in §3.2 (Figure 7) and §3.4 (Figure 9) were actually obtained by uniformly sampling the Euler angles θ , constrained to $(\theta_3, \theta_2, \theta_1) \in [0, 2\pi[\times [0, \frac{\pi}{2}[\times [0, 2\pi[$ for 5j0n. Our conclusions would be identical if orientations were uniformly sampled from $\mathbf{SO}(3)$ instead.

Dataset	P	P^2	Used pairs
Training	2,512 (50%)	6,310,144	63,101
Validation	838 (17%)	702,244	7,022
Test	1,650 (33%)	2,722,500	2,722,500

Table 1: Split of $P = 5,000$ projections in training, validation, and test subsets.

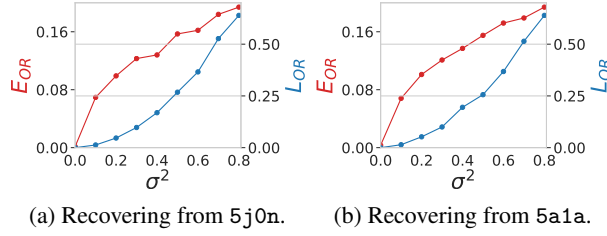
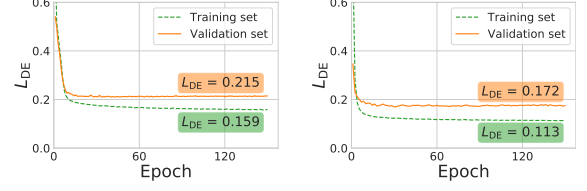
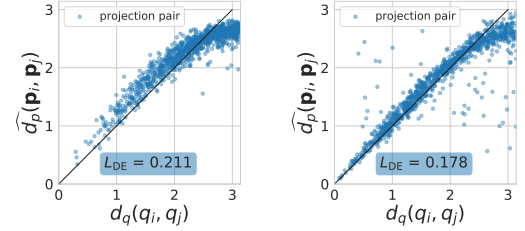


Figure 7: Orientation recovery from perturbed distances.



(a) Loss converged on 5j0n (left) and 5a1a (right).



(b) Relationship between \hat{d}_p and d_q on 1,000 pairs sampled from the test sets of 5j0n (left) and 5a1a (right).

Figure 8: Distance learning.

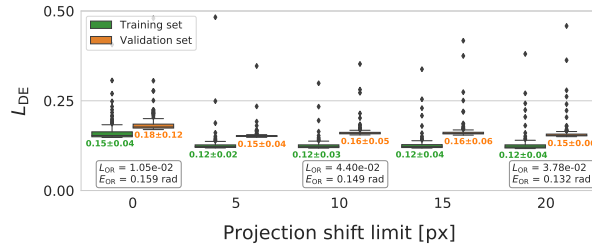
3.4 Sensitivity of distance learning to perturbations in the projections

We first demonstrated that the learning of distances is insensitive to off-centering shifts (Figure 9a), which is expected given the shift invariance built in our SiameseNN (see §2.2).

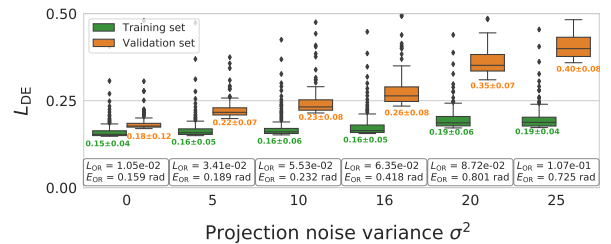
As we cannot—or do not yet know how to—build noise invariance in the SiameseNN architecture, we trained the SiameseNN on noisy projections and evaluated whether it could learn to treat noise as an irrelevant information. Figure 9b shows $E_{OR} \approx 0.16$ radians ($\approx 9^\circ$) for noiseless projections and $E_{OR} \approx 0.42$ radians ($\approx 24^\circ$) for a more realistic noise variance of $\sigma^2 = 16$ (with signal-to-noise ratio of -12 dB). Whereas a naive distance function (*e.g.*, an Euclidean distance) would be extremely sensitive to noise, the SiameseNN mostly learned to discard it. Moreover, the observed overfitting indicates that more training data should further decrease the sensitivity of the SiameseNN to noise.

Note that we did not evaluate sensitivity to the PSF at this stage but expect a similar behavior.

Here again (§3.2), we observed that (i) the estimation of more accurate distances (a smaller L_{DE}) leads to the recovery of more accurate orientations (a smaller L_{OR} and E_{OR}), and that (ii) an higher recovery loss L_{OR} induces an higher error E_{OR} .

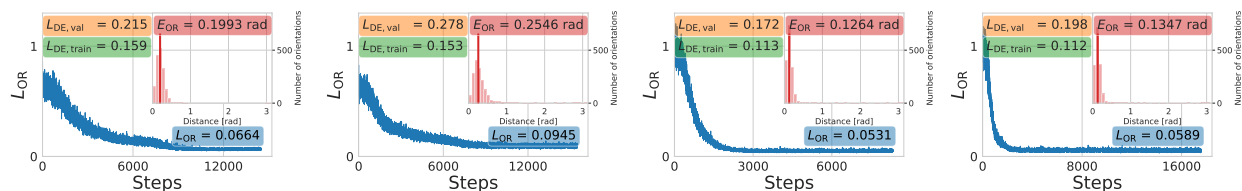


(a) Learning from shifted projections $\{S_{t_i} \mathbf{P}_{\theta_i} \mathbf{x}\}$, with shifts t_{i_1} and t_{i_2} sampled from a triangular distribution with mean 0 and of increasing limits. Learning is not harder as projections get shifted farther, because shift invariance is built into the convolutional architecture of \mathcal{G}_w .



(b) Learning from noisy projections $\{\mathbf{P}_{\theta_i} \mathbf{x} + \mathbf{n}\}$, with white noise $\mathbf{n} \sim \mathcal{N}(0, \sigma^2 \mathbf{I})$ of increasing variance σ^2 . Learning is harder as projections get noisier, because noise invariance is not built into the architecture of \mathcal{G}_w .

Figure 9: Sensitivity of distance learning to perturbations in the projections of 5j0n. The box plots show the distance learning loss L_{DE} (3) (the distribution is taken over epochs). Boxes show the orientation recovery loss L_{OR} (4) and error E_{OR} (5).



(a) Noiseless projections of 5j0n. (b) Noisy projections of 5j0n. (c) Noiseless projections of 5a1a. (d) Noisy projections of 5a1a.

Figure 10: Distance learning and orientation recovery from estimated distances. The green and orange boxes show L_{DE} (3) on the training and validation sets. The blue curve shows the evolution of the recovery loss until convergence, with the minimum L_{OR} (4) highlighted. The red histogram shows the errors in the recovered orientations $\{d_q(q_i, \mathbf{T}\hat{q}_i)\}$, with the mean E_{OR} (5) highlighted.

3.5 Orientation recovery and reconstruction of density maps

As a proof-of-concept, we attempted to solve the full inverse problem posed by (1), *i.e.*, to reconstruct the density maps $\hat{\mathbf{x}}$ from sets of projections $\{\mathbf{p}_i\}$ and their orientations $\{\hat{q}_i\}$ recovered through the proposed method. It is worth noting that, at this stage of development, we only trained the SiameseNN on projections originating from the protein we were attempting to reconstruct. In addition, reconstruction was performed with a direct reconstruction algorithm (ASTRA’s GPU implementation of the CGLS algorithm) rather than with a robust iterative method. This is obviously a specific experimental case that only partially shines light on the applicability of the method in real situations; this is discussed in §4.

Figure 10a shows the recovery of orientations from distances that were estimated from noiseless projections of 5j0n. A mean error of $E_{OR} \approx 0.20$ radians ($\approx 11^\circ$) in the recovered orientations led to a reconstruction with a resolution of 12.2Å at a Fourier shell coefficient (FSC) of 0.5, shown in Figure 11c.

As predicted by our other experiments, corrupting the projections with noise ($\sigma^2 = 16$) negatively impacts the quality of the recovered orientations (Figure 10b); the obtained mean error is then $E_{OR} \approx 0.25$ radians ($\approx 14^\circ$). Unsurprisingly, this leads to a reconstruction with a lower resolution of 15.2Å, shown in Figure 11d. (Note that reconstruction was here obtained from the noiseless projections, the goal being to evaluate only the impact of orientation mis-estimation.)

Finally, Figure 10c and 10d show the recovery of orientations from noiseless and noisy projections of 5a1a. A mean error of $E_{OR} \approx 0.13$ radians ($\approx 7^\circ$) in both cases led to reconstructions with resolutions of 8.0Å and 9.6Å, shown in Figure 11h and 11i. Distance estimation, orientation recovery, and reconstruction performed better on 5a1a than 5j0n because its ground-truth density is of higher resolution.

These results tend to indicate that a reasonable first structure can be reconstructed from projections whose orientations have been recovered through our method.

4 Discussion

In this work, we explored the use of distance learning between pairs of 2D cryo-EM projections from a 3D protein structure to infer the unknown orientation at which each projection was imaged from. Our two-step method relies on the training of a SiameseNN to estimate pairwise distances between unseen projections, followed by the recovery of the orientations from these distances through an appropriate minimization scheme.

At the current stage of development, the method has been evaluated on synthetic datasets for two different proteins. The results provide key insights on the viability of the proposed scheme. First, they demonstrate that a SiameseNN can learn a distance function between projections that estimates the difference in their orientation (§3.3) and that is invariant to off-centering shifts and robust to increasing levels of noise (§3.4)—an important condition in cryo-EM. Second, they demonstrate that an accurate estimation of distances leads to an accurate recovery of orientations (§3.2, §3.4). Finally, our method was able to recover orientations with an error of 0.12 to 0.25 radians (7 to 14°)—leading to an initial volume with a resolution of 8 to 15Å (§3.5). In summary, the more accurate the estimated distances, the more precise the recovered orientations, and, ultimately, the higher-resolution the reconstructed volume.

While the method is not yet at the stage where it can be deployed in practice, we believe that a series of developments could help it become a more relevant contributor for single-particle cryo-EM reconstruction.⁷ As previously discussed,

⁷Note that the present project will not be further continued by its authors due to other professional occupations. Hence, we strongly encourage anyone interested to build on these ideas and, hopefully, make it a practical tool.

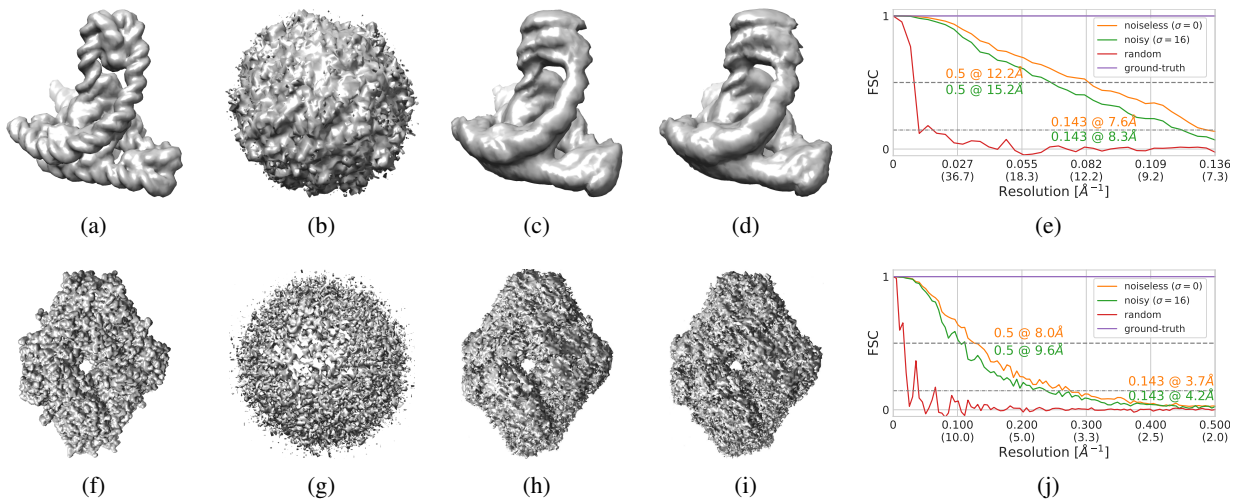


Figure 11: Density maps \hat{x} reconstructed from (a,f) ground-truth orientations, (b,g) random orientations, (c,h) orientations recovered from noiseless projections, and (d,i) orientations recovered from noisy projections. The Fourier shell correlation (FSC) curves in (e,j) indicate the resolutions of the densities reconstructed from recovered orientations (w.r.t. ground-truth densities, shown in Figure 5c,d).

the results underline the importance of learning an accurate distance estimator. In this regard, the performance of the SiameseNN could be improved in several ways. First, the architecture of the SiameseNN’s twin convolutional neural networks should be expanded and tuned. Second, the training of the SiameseNN could be improved, perhaps by providing more supervision by separately predicting the differences in direction (θ_2, θ_1) and in-plane angle θ_3 .

Importantly, the SiameseNN would be better trained on a more exhaustive and diverse cryo-EM dataset. Indeed, the success of the SiameseNN as a faithful estimator of relative orientations eventually relies on our capacity to generate a synthetic training dataset whose data distribution is diverse enough to cover that of unseen projection datasets. Such realistic cryo-EM projections could be generated by relying on a more expressive formulation of the cryo-EM physics and taking advantage of the thousands of atomic models available in the PDB. In particular, a necessary extension will be to include the effects of the PSF when generating training data and evaluate its impact on the SiameseNN.

A final phase of tests before deploying the method on real cryo-EM measurements will be to extensively test the method on “unseen proteins”, *i.e.*, proteins whose simulated projections have never been seen by the SiameseNN. In this regard, an interesting aspect of our method is that the twin networks within the SiameseNN intrinsically predict the *relationship* between projections, allowing the SiameseNN as a whole to abstract the particular volume. Learning benefits from the profound structural similarity shared by proteins—after all, they are all derived from the same 21 building blocks.

Acknowledgments

The authors are thankful to Dr. Matthieu Simeoni (EPFL) and Dr. Julien Fageot (EPFL) for insightful discussions.

References

- [1] J. Dubochet, M. Adrian, J.-J. Chang, J.-C. Homo, J. Lepault, A. W. McDowell, and P. Schultz, “Cryo-electron microscopy of vitrified specimens,” *Quarterly Reviews of Biophysics*, vol. 21, no. 2, pp. 129–228, 1988.
- [2] J. Frank, *Three-dimensional electron microscopy of macromolecular assemblies: Visualization of biological molecules in their native state*. Oxford University Press, 2006.
- [3] Nature, “Method of the year 2015,” *Nature Methods*, vol. 13, no. 1, 2016.
- [4] F. Natterer, *The mathematics of computerized tomography*. Society for Industrial and Applied Mathematics, jan 2001.
- [5] F. DiMaio, D. A. Kondrashov, E. Bitto, A. Soni, C. A. Bingman, G. N. Phillips, and J. W. Shavlik, “Creating protein models from electron-density maps using particle-filtering methods,” *Bioinformatics*, vol. 23, no. 21, pp. 2851–2858, Nov. 2007. [Online]. Available: <https://academic.oup.com/bioinformatics/article/23/21/2851/374177>

- [6] M. Vulović, R. B. Ravelli, L. J. van Vliet, A. J. Koster, I. Lazić, U. Lücken, H. Rullgård, O. Öktem, and B. Rieger, “Image formation modeling in cryo-electron microscopy,” *Journal of Structural Biology*, vol. 183, no. 1, pp. 19–32, Jul. 2013.
- [7] H. Rullgård, L.-G. Öfverstedt, S. Masich, B. Daneholt, and O. Öktem, “Simulation of transmission electron microscope images of biological specimens,” *Journal of Microscopy*, vol. 243, no. 3, pp. 234–256, 2011.
- [8] P. A. Penczek, R. A. Grassucci, and J. Frank, “The ribosome at improved resolution: New techniques for merging and orientation refinement in 3D cryo-electron microscopy of biological particles,” *Ultramicroscopy*, vol. 53, no. 3, pp. 251–270, 1994.
- [9] T. Baker and R. Cheng, “A model-based approach for determining orientations of biological macromolecules imaged by cryoelectron microscopy,” *Journal of Structural Biology*, vol. 116, no. 1, pp. 120–130, 1996. [Online]. Available: <http://www.sciencedirect.com/science/article/pii/S1047847796900209>
- [10] A. P. Dempster, N. M. Laird, and D. B. Rubin, “Maximum likelihood from incomplete data via the EM algorithm,” *Journal of the Royal Statistical Society. Series B (Methodological)*, vol. 39, no. 1, pp. 1–38, 1977.
- [11] F. J. Sigworth, “A maximum-likelihood approach to single-particle image refinement,” *Journal of structural biology*, vol. 122, no. 3, pp. 328–339, 1998.
- [12] S. Scheres, “A bayesian view on cryo-EM structure determination,” *Journal of molecular biology*, vol. 415, no. 2, pp. 406–418, 2012.
- [13] M. Zehni, L. Donati, E. Soubies, Z. J. Zhao, and M. Unser, “Joint Angular Refinement and Reconstruction for Single-Particle Cryo-EM,” *IEEE Transactions on Image Processing*, 2020.
- [14] C. O. S. Sorzano, R. Marabini, A. Pascual-Montano, S. H. Scheres, and J. M. Carazo, “Optimization problems in electron microscopy of single particles,” *Annals of Operations Research*, vol. 148, no. 1, pp. 133–165, 2006.
- [15] R. Henderson, A. Sali, M. L. Baker, B. Carragher, B. Devkota, K. H. Downing, E. H. Egelman, Z. Feng, J. Frank, N. Grigorieff, W. Jiang, S. J. Ludtke, O. Medalia, P. A. Penczek, P. B. Rosenthal, M. G. Rossmann, M. F. Schmid, G. F. Schröder, A. C. Steven, D. L. Stokes, J. D. Westbrook, W. Wriggers, H. Yang, J. Young, H. M. Berman, W. Chiu, G. J. Kleywegt, and C. L. Lawson, “Outcome of the first electron microscopy validation task force meeting,” *Structure*, vol. 20, no. 2, pp. 205–214, 2012.
- [16] A. Singer and F. J. Sigworth, “Computational methods for single-particle electron cryomicroscopy,” *Annual Review of Biomedical Data Science*, vol. 3, 2020.
- [17] Z. Kam, “The reconstruction of structure from electron micrographs of randomly oriented particles,” in *Electron Microscopy at Molecular Dimensions*. Springer, 1980, pp. 270–277.
- [18] D. B. Salzman, “A method of general moments for orienting 2d projections of unknown 3d objects,” *Computer vision, graphics, and image processing*, vol. 50, no. 2, pp. 129–156, 1990.
- [19] A. Goncharov, “Integral geometry and three-dimensional reconstruction of randomly oriented identical particles from their electron microphotos,” *Acta Applicandae Mathematica*, vol. 11, no. 3, pp. 199–211, 1988.
- [20] N. Sharon, J. Kileel, Y. Khoo, B. Landa, and A. Singer, “Method of moments for 3-d single particle ab initio modeling with non-uniform distribution of viewing angles,” *Inverse Problems*, 2019.
- [21] M. Van Heel, “Angular reconstitution: a posteriori assignment of projection directions for 3d reconstruction,” *Ultramicroscopy*, vol. 21, no. 2, pp. 111–123, 1987.
- [22] S. P. Mallick, S. Agarwal, D. J. Kriegman, S. J. Belongie, B. Carragher, and C. S. Potter, “Structure and view estimation for tomographic reconstruction: A bayesian approach,” in *2006 IEEE Computer Society Conference on Computer Vision and Pattern Recognition (CVPR’06)*, vol. 2. IEEE, 2006, pp. 2253–2260.
- [23] A. Singer, R. R. Coifman, F. J. Sigworth, D. W. Chester, and Y. Shkolnisky, “Detecting consistent common lines in cryo-EM by voting,” *Journal of structural biology*, vol. 169, no. 3, pp. 312–322, 2010.
- [24] L. Wang, A. Singer, and Z. Wen, “Orientation determination of cryo-EM images using least unsquared deviations,” *SIAM journal on imaging sciences*, vol. 6, no. 4, pp. 2450–2483, 2013.
- [25] I. Greenberg and Y. Shkolnisky, “Common lines modeling for reference free ab-initio reconstruction in cryo-EM,” *Journal of structural biology*, vol. 200, no. 2, pp. 106–117, 2017.
- [26] G. Pragier and Y. Shkolnisky, “A common lines approach for ab initio modeling of cyclically symmetric molecules,” *Inverse Problems*, vol. 35, no. 12, p. 124005, 2019.
- [27] A. Punjani, J. L. Rubinstein, D. J. Fleet, and M. A. Brubaker, “cryoSPARC: Algorithms for rapid unsupervised cryo-EM structure determination,” *Nature Methods*, vol. 14, no. 3, p. 290, 2017.

- [28] M. Zehni, S. Huang, I. Dokmanić, and Z. Zhao, “Distance retrieval from unknown view tomography of 2d point sources,” *Electronic Imaging*, vol. 2019, no. 13, pp. 134–1, 2019.
- [29] N. Miolane, F. Poitevin, Y.-T. Li, and S. Holmes, “Estimation of orientation and camera parameters from cryo-electron microscopy images with variational autoencoders and generative adversarial networks,” 2019.
- [30] Y. LeCun, Y. Bengio, and G. Hinton, “Deep learning,” *nature*, vol. 521, no. 7553, pp. 436–444, 2015.
- [31] R. R. Coifman, Y. Shkolnisky, F. J. Sigworth, and A. Singer, “Graph laplacian tomography from unknown random projections,” *IEEE Transactions on Image Processing*, vol. 17, no. 10, pp. 1891–1899, 2008.
- [32] C. Sorzano, R. Marabini, J. Vargas, J. Otón, J. Cuenca-Alba, A. Quintana, J. de la Rosa-Trevín, and J. Carazo, “Interchanging geometry conventions in 3dem: mathematical context for the development of standards,” in *Computational Methods for Three-Dimensional Microscopy Reconstruction*. New York, NY: Springer New York, 2014, pp. 7–42. [Online]. Available: https://doi.org/10.1007/978-1-4614-9521-5_2
- [33] D. Q. Huynh, “Metrics for 3D rotations: Comparison and analysis,” *Journal of Mathematical Imaging and Vision*, vol. 35, no. 2, pp. 155–164, 2009.
- [34] S. Chopra, R. Hadsell, and Y. LeCun, “Learning a similarity metric discriminatively, with application to face verification,” in *2005 IEEE Computer Society Conference on Computer Vision and Pattern Recognition (CVPR’05)*, vol. 1. IEEE, 2005, pp. 539–546.
- [35] D. Yi, Z. Lei, S. Liao, and S. Z. Li, “Deep metric learning for person re-identification,” in *2014 22nd International Conference on Pattern Recognition*. IEEE, 2014, pp. 34–39.
- [36] M. A. Cox and T. F. Cox, “Multidimensional scaling,” in *Handbook of data visualization*. Springer, 2008, pp. 315–347.
- [37] J. B. Tenenbaum, V. d. Silva, and J. C. Langford, “A global geometric framework for nonlinear dimensionality reduction,” *Science*, vol. 290, no. 5500, pp. 2319–2323, 2000. [Online]. Available: <https://science.sciencemag.org/content/290/5500/2319>
- [38] S. T. Roweis and L. K. Saul, “Nonlinear dimensionality reduction by locally linear embedding,” *Science*, vol. 290, no. 5500, pp. 2323–2326, 2000.
- [39] M. Belkin and P. Niyogi, “Laplacian eigenmaps for dimensionality reduction and data representation,” *Neural computation*, vol. 15, no. 6, pp. 1373–1396, 2003.
- [40] L. Van der Maaten and G. Hinton, “Visualizing data using t-sne,” *Journal of machine learning research*, vol. 9, no. 11, 2008.
- [41] L. McInnes, J. Healy, and J. Melville, “Umap: Uniform manifold approximation and projection for dimension reduction,” *arXiv preprint arXiv:1802.03426*, 2018.
- [42] I. Dokmanic, R. Parhizkar, J. Ranieri, and M. Vetterli, “Euclidean distance matrices: essential theory, algorithms, and applications,” *IEEE Signal Processing Magazine*, vol. 32, no. 6, pp. 12–30, 2015.
- [43] A. Bartesaghi, A. Merk, S. Banerjee, D. Matthies, X. Wu, J. L. Milne, and S. Subramaniam, “2.2 Å resolution cryo-EM structure of β -galactosidase in complex with a cell-permeant inhibitor,” *Science*, vol. 348, no. 6239, pp. 1147–1151, 2015.
- [44] G. Laxmikanthan, C. Xu, A. F. Brilot, D. Warren, L. Steele, N. Seah, W. Tong, N. Grigorieff, A. Landy, and G. D. Van Duyn, “Structure of a holliday junction complex reveals mechanisms governing a highly regulated dna transaction,” *Elife*, vol. 5, p. e14313, 2016.
- [45] E. F. Pettersen, T. D. Goddard, C. C. Huang, G. S. Couch, D. M. Greenblatt, E. C. Meng, and T. E. Ferrin, “Ucsf chimera—a visualization system for exploratory research and analysis,” *Journal of Computational Chemistry*, vol. 25, no. 13, pp. 1605–1612, 2004.
- [46] W. van Aarle, W. J. Palenstijn, J. De Beenhouwer, T. Altantzis, S. Bals, K. J. Batenburg, and J. Sijbers, “The ASTRA toolbox: A platform for advanced algorithm development in electron tomography,” *Ultramicroscopy*, vol. 157, pp. 35–47, 2015.
- [47] C. Sorzano, L. De La Fraga, R. Clackdoyle, and J. Carazo, “Normalizing projection images: A study of image normalizing procedures for single particle three-dimensional electron microscopy,” *Ultramicroscopy*, vol. 101, no. 2-4, pp. 129–138, 2004.
- [48] H. Shigematsu and F. Sigworth, “Noise models and cryo-EM drift correction with a direct-electron camera,” *Ultramicroscopy*, vol. 131, pp. 61–69, 2013.
- [49] T. Tieleman and G. Hinton, “Lecture 6.5-rmsprop: Divide the gradient by a running average of its recent magnitude,” *COURSERA: Neural networks for machine learning*, vol. 4, no. 2, pp. 26–31, 2012.

- [50] D. P. Kingma and J. Ba, “Adam: A method for stochastic optimization,” *arXiv preprint arXiv:1412.6980*, 2014.
- [51] H. B. McMahan, D. Golovin, S. Chikkerur, D. Liu, M. Wattenberg, A. M. Hrafinkelsson, T. Boulos, J. Kubica, G. Holt, D. Sculley, M. Young, D. Ebner, J. Grady, L. Nie, T. Phillips, and E. Davydov, “Ad click prediction: a view from the trenches,” in *Proceedings of the 19th ACM SIGKDD international conference on Knowledge discovery and data mining - KDD '13*. ACM Press, 2013, p. 1222. [Online]. Available: <http://dl.acm.org/citation.cfm?doid=2487575.2488200>

A Sampling of orientations

Figure 12 shows four distributions of orientations and the distributions of distances they induce. As shorter distances are under-sampled, we uniformly resampled the distances to avoid biasing the training of our distance estimator.

While we control the distributions of orientations and distances to facilitate distance learning, we cannot control them when recovering orientations of a given set of projections. Comparing Figure 13a with 10a, and 13b with 11e, shows that the recovered orientations and the reconstructed density are barely affected by a non-uniform sampling of orientations—a condition that might happen in real cryo-EM acquisitions.

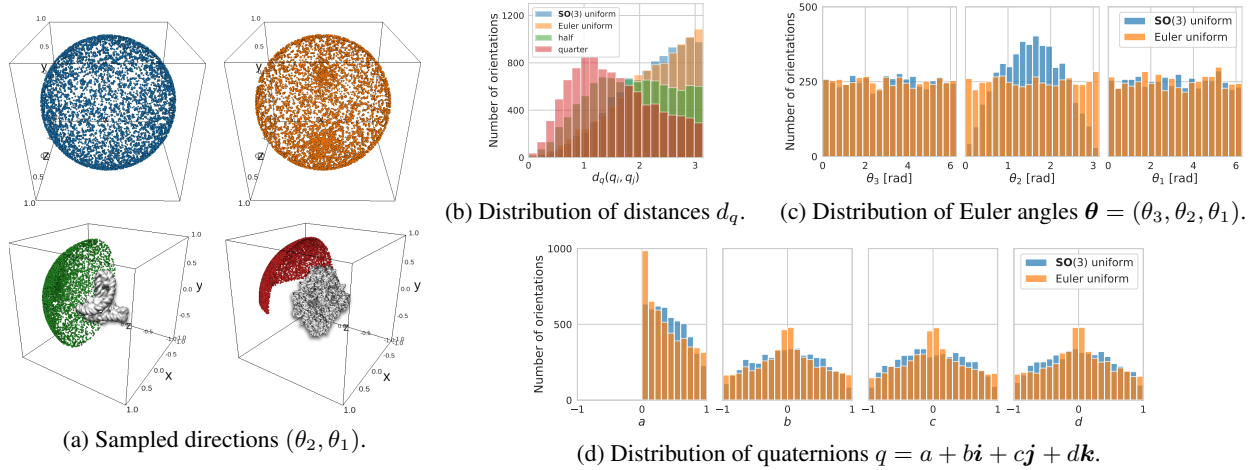


Figure 12: Sampling of orientations from four distributions: (blue) uniform on $\text{SO}(3)$, (orange) uniform on Euler angles, (green) Euler uniform restricted to half the directions $(\theta_2, \theta_1) \in [0, \frac{\pi}{2}] \times [0, 2\pi]$, and (red) $\text{SO}(3)$ uniform restricted to a quarter of the directions $(\theta_2, \theta_1) \in [0, \frac{\pi}{2}] \times [0, \pi]$.

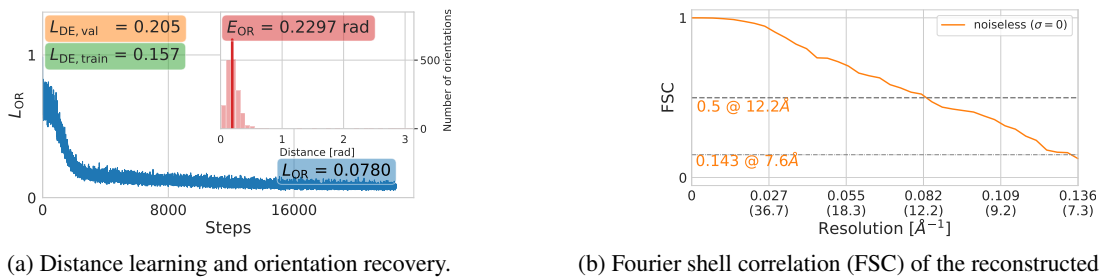


Figure 13: Orientation recovery and density reconstruction from noiseless projections of 5j0n acquired from non-uniformly sampled orientations (uniformly sampled Euler angles, Figure 12 (orange)).

B Orientation recovery from exact distances

To verify that the lack of a convexity guarantee for (4) and the sampling of the sum are non-issues in practice, we attempted orientation recovery under exact distance estimation $\hat{d}_p(\mathbf{p}_i, \mathbf{p}_j) = d_q(q_i, q_j)$. Orientations were perfectly recovered; Figure 14 shows the convergence of L_{OR} to zero. Figure 15 shows how (5) could then perfectly align the recovered and true orientations—leading to $E_{OR} = 0$. It illustrates how alignment is necessary to evaluate the performance of orientation recovery.

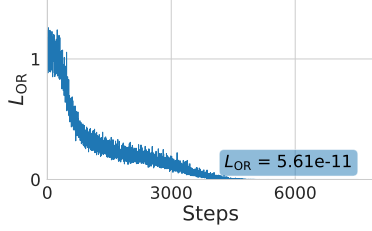
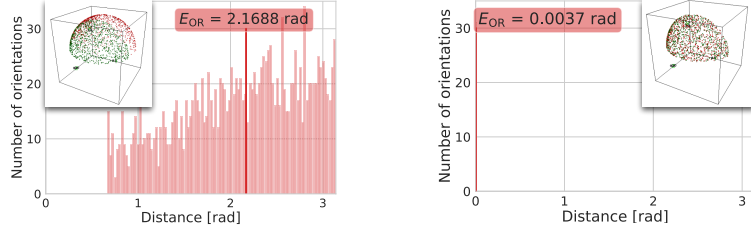


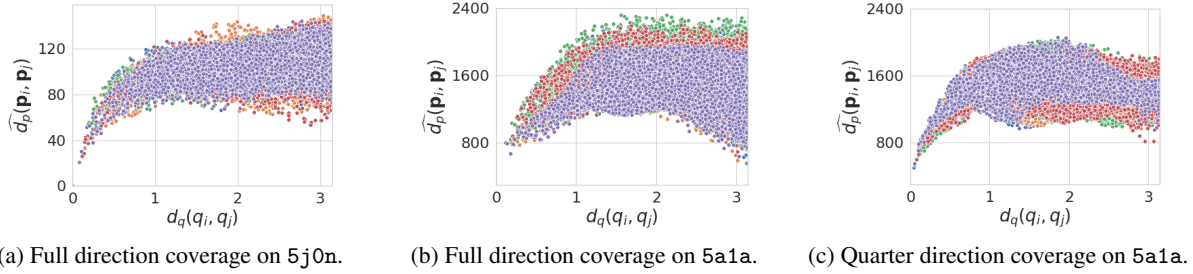
Figure 14: Example of perfect orientation recovery (for 5a1a). The loss L_{OR} (4) converges to zero when the distance estimation is perfect, *i.e.*, $\hat{d}_p(\mathbf{p}_i, \mathbf{p}_j) = d_q(q_i, q_j)$.



(a) Orientations before alignment.

(b) Orientations after alignment.

Figure 15: Example of perfect alignment (5) after a perfect recovery (4). The red histogram shows the errors (a) $\{d_q(q_i, \hat{q}_i)\}$ and (b) $\{d_q(q_i, \mathbf{T}\hat{q}_i)\}$, with the mean E_{OR} highlighted. True (green) and recovered (green) directions are shown in the insert. While both colors are seen in (b), they are superimposed.



(a) Full direction coverage on 5j0n.

(b) Full direction coverage on 5a1a.

(c) Quarter direction coverage on 5a1a.

Figure 16: Euclidean distance between projections $\hat{d}_p(\mathbf{p}_i, \mathbf{p}_j) = \|\mathbf{p}_i - \mathbf{p}_j\|_2$ versus their actual relative orientation $d_q(q_i, q_j)$. We randomly selected 5 projections from $P = 5,000$: each color represents the distances between one of those and all the others.

C Euclidean distance between projections

We evaluate $\hat{d}_p(\mathbf{p}_i, \mathbf{p}_j) = \|\mathbf{p}_i - \mathbf{p}_j\|_2$ (*i.e.*, the Euclidean distance) as a baseline distance estimator. Figure 16 shows the relationship between \hat{d}_p and d_q . Two main observations can be made from this experiment. First, as suspected, \hat{d}_p fails to be a consistent predictor of d_q , even in the simple imaging conditions considered here (no noise, no shift, no PSF). In particular, the larger the orientation distance d_q , the poorer the predictive ability of \hat{d}_p (the plot plateaus). Second, because 5a1a has D2 symmetries, two projections might be identical while not having been acquired from the same orientation. Restricting directions to a quarter captures only one of four identical projections, solving the issue.

D SiameseNN: feature distance and embedding dimension

There are multiple options for a distance function d_f between two features $\mathbf{f}_i = \mathcal{G}_w(\mathbf{p}_i) \in \mathbb{R}^{n_f}$. Figure 17a compares the use of the Euclidean distance $d_f(\mathbf{f}_i, \mathbf{f}_j) = \|\mathbf{f}_i - \mathbf{f}_j\|_2$ and the cosine distance $d_f(\mathbf{f}_i, \mathbf{f}_j) = 2 \arccos\left(\frac{\langle \mathbf{f}_i, \mathbf{f}_j \rangle}{\|\mathbf{f}_i\| \|\mathbf{f}_j\|}\right)$. The cosine distance results in a lower L_{DE} , which makes \hat{d}_p a better estimator of d_q . This superiority of the cosine distance is likely due to its capacity to model the elliptic geometry of $\mathbf{SO}(3)$, a feat the Euclidean distance does not achieve, the Euclidean space being neither periodic nor curved.

Figure 17b shows the performance of our distance estimator \hat{d}_p depending on the size n_f of the feature space. It clearly indicates that a space of $n_f = 4$ dimensions is insufficient to represent the variability of projections. That is a motivation to embed the projections in a space of higher dimensions that can represent more variations than the orientation, and can abstract that variation by solely considering the distances between the embedded projections $\mathbf{f}_i = \mathcal{G}_w(\mathbf{p}_i)$. While our choice of $n_f = 512$ might be overkill ($n_f = 16$ seems sufficient), it is not penalizing.

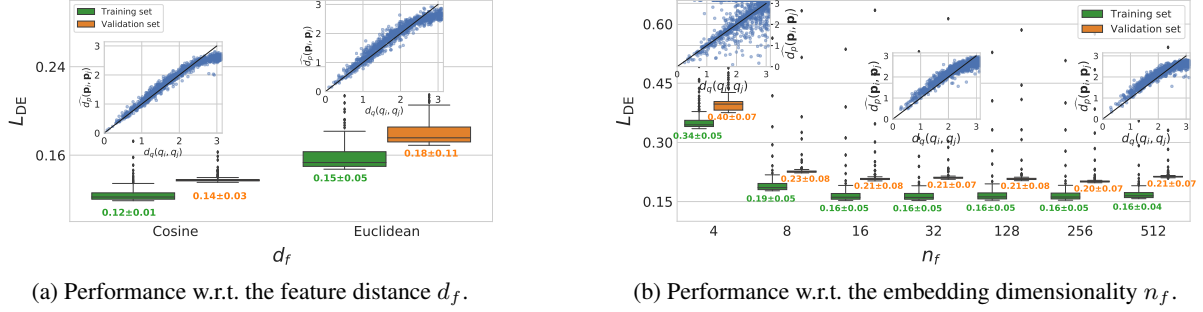


Figure 17: Performance of our distance estimator \hat{d}_p w.r.t. two design choices. The box plots show the distance learning loss L_{DE} (3). The inserted plots show the relationship between $d_p(\mathbf{p}_i, \mathbf{p}_j) = d_f(\mathcal{G}_w(\mathbf{p}_i), \mathcal{G}_w(\mathbf{p}_j))$ and $d_q(q_i, q_j)$ on 1,000 pairs sampled from $5j0n$.

E Convolutional neural network architecture

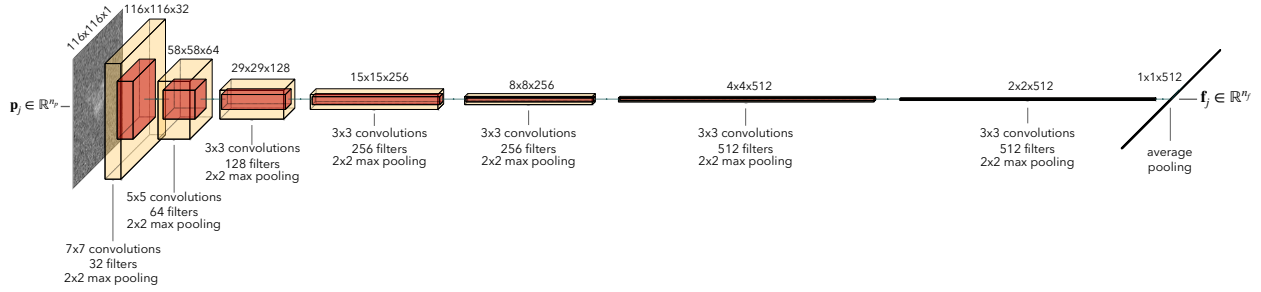


Figure 18: Architecture of \mathcal{G}_w , the convolutional neural network that extracts feature vectors $\mathbf{f}_j = \mathcal{G}_w(\mathbf{p}_j) \in \mathbb{R}^{n_f}$ from projections $\mathbf{p}_j \in \mathbb{R}^{n_p}$. While $n_f = 512$ and $n_p = 116 \times 116$ in our experiments, \mathcal{G}_w can accommodate any image size thanks to the global average pooling layer.